Continuum-particle hybrid coupling for mass, momentum, and energy transfers in unsteady fluid flow

R. Delgado-Buscalioni* and P. V. Coveney†
Centre for Computational Science, Department of Chemistry, University College London, London, United Kingdom
(Received 1 November 2002; published 11 April 2003)

The aim of hybrid methods in simulations is to communicate regions with disparate time and length scales. Here, a fluid described at the atomistic level within an inner region *P* is coupled to an outer region *C* described by continuum fluid dynamics. The matching of both descriptions of matter is made across an overlapping region and, in general, consists of a two-way coupling scheme ($C \rightarrow P$ and $P \rightarrow C$) that conveys mass, momentum, and energy fluxes. The contribution of the hybrid scheme hereby presented is twofold. First, it treats unsteady flows and, more importantly, it handles energy exchange between both *C* and *P* regions. The implementation of the $C \rightarrow P$ coupling is tested here using steady and unsteady flows with different rates of mass, momentum and energy exchange. In particular, relaxing flows described by linear hydrodynamics (transversal and longitudinal waves) are most enlightening as they comprise the whole set of hydrodynamic modes. Applying the hybrid coupling scheme after the onset of an initial perturbation, the cell-averaged Fourier components of the flow variables in the *P* region (velocity, density, internal energy, temperature, and pressure) evolve in excellent agreement with the hydrodynamic trends. It is also shown that the scheme preserves the correct rate of entropy production. We discuss some general requirements on the coarse-grained length and time scales arising from both the characteristic microscopic and hydrodynamic scales.

DOI: 10.1103/PhysRevE.67.046704 PACS number(s): 02.70.−c, 47.11.+j, 47.10.+g, 68.65.−k

I. INTRODUCTION

A wide range of systems with important applications are governed by a fine interplay between the atomistic processes occurring within a small region of the system and the slow dynamics occurring within the bulk. A large list of examples arise in complex flows near interfaces (polymers or colloids near surfaces, wetting, drop formation, melting, crystal growth from a fluid phase, moving interfaces of immiscible fluids or membranes, to name only a few). The computational expense of realistic-size simulations of these problems via standard molecular dynamics (MD) is prohibitive, and such kind of studies require new algorithms that can retain the benefit of the atomistic description of matter where it is really needed, while treating the bulk of the system by much less costly continuum fluid mechanics methods.

Several hybrid algorithms of this sort have been proposed in the recent literature. In general, to couple the particle region *P* and the continuum region *C*, such hybrid schemes use an overlapping region comprised of two buffers $C \rightarrow P$ and $P \rightarrow C$, which account for the two-way transfer of information: from *C* to *P* and vice versa (see Fig. 1). While the $P \rightarrow C$ transfer essentially consists of a coarse-graining procedure, at $C \rightarrow P$ one needs to reconstruct the dynamics of a large collection of particles with only the limited prescription from the *C* region as input. Moreover, in performing this reconstruction, the number of unphysical artifacts added (as Maxwell demons) should be minimized as far as possible. This task is very complicated and represents, in fact, the main part of any hybrid scheme.

Hybrid algorithms for fluids are relatively recent. The elegant method introduced by Garcia *et al.* [1] for rarefied gases couples fluxes arising from a direct simulation Monte Carlo (DSMC) scheme to another region described by computational fluid dynamics (CFD). The DSMC is set at the finest grid scale of an adaptive mesh refinement hierarchy, while a CFD semi-implicit solver is used at the upper level scales. In passing, we note that the scheme may, in principle, be implemented using an (MD-continuum) liquid description, although in this case the *C* solver must be completely explicit to avoid having to change the particle's energy in the iterations of the implicit scheme.

In the case of liquids, the state of the art is relatively less developed due to the complications arising from the interparticle forces. A pioneering work by O'Connell and Thompson [2] coupled momentum by imposing the local continuum velocity at $C \rightarrow P$ via a crude constraint Lagrangian dynamics.

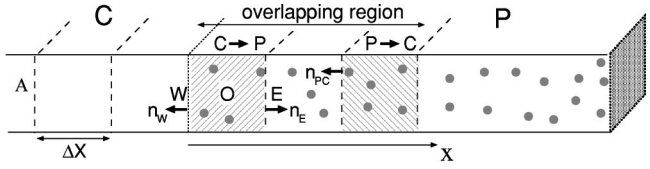

FIG. 1. (a) Spatial decomposition in our hybrid scheme. In this example, the *P* region is adjacent to a physical surface represented by the rightmost shaded area. The continuum region spans the space to the left at some distance from the surface. The overlapping region consists of a $C \rightarrow P$ cell, where the *C* flow is communicated to *P*, and a $P \rightarrow C$ cell, where particle-averaged fluxes are injected into the *C* flow. Dashed lines delimit the control cells of the *C* solver, with area *A* and grid spacing ΔX. The letters *O*, *W*, and *E* denote the center of a cell and its west and east surfaces, respectively. The main cell's vectors ($\mathbf{n}_W$, $\mathbf{n}_E$, and $\mathbf{n}_{PC}$) have been indicated (see text).

*Email address: R.Delgado-Buscalioni@ucl.ac.uk
†Email address: P.V.Coveney@ucl.ac.uk

Hadjiconstantinou and Patera [3] introduced a reservoir region to impose boundary conditions on the P region (this reservoir being the equivalent of the $C \rightarrow P$ domain defined here). While in residence in the reservoir, particles were given, at each time step, a velocity drawn from a Maxwellian distribution with mean and variance consistent with the velocity and temperature of the C flow. To obtain the boundary condition for the C region, the authors used a low order polynomial to smoothen the field variables derived from P at the $P \rightarrow C$ region. In order to match the boundary conditions for both the P and C regions, Hadjiconstantinou and Patera [3] implemented an iterative scheme (based on the Schwarz alternating method) that is suitable for steady incompressible flows. Liao and co-workers [4] proposed a sophisticated method (called the thermodynamic field estimator) to extract continuum fields from the particle data by means of maximum likehood inference. This idea may be used to ameliorate the $P \rightarrow C$ coupling when the flow presents large gradients, albeit at a rather large computational cost. To transfer momentum on the P region, Liao and co-workers [4] proposed a new Maxwell demon, called reflecting particle method. A drawback is that the pressure gradient is then an outcome of the simulation, rather than an input. Finally, Flekkoy *et al.* [5] used the idea of coupling through fluxes and also implemented mass transfer. However, energy transfer was still not allowed and only steady flows were considered. The main purpose of the present work is to broaden the scope of such hybrid schemes towards a general description allowing mass, momentum, and energy coupling in unsteady flows.

A question of central interest is to decide what kind of information needs to be transferred at $C \rightarrow P$ and $P \rightarrow C$. There are essentially two possibilities, to transfer either generalized forces (fluxes of conserved quantities) or the local values of the averaged variables. Both kinds of approaches can be found in the published literature. Here, in the context of energy transfer, we show that under unsteady flows it is not sufficient to impose the local C quantities at the boundary of P; instead, it is necessary to couple through fluxes. Another possible benefit of flux coupling was pointed out by Flekkoy *et al.* [5] who stated that this procedure transcends the problem of working with fluids whose constitutive relations may be only partially or incompletely known. Although we agree that the flux-based coupling is the correct matching procedure, we show nevertheless that if the transport coefficients at C and P are disparate enough, the hybrid scheme fails to couple the time evolution of both domains. Hence, in such cases, the evaluation of transport coefficients (using standard microscopic techniques, at least for the range of densities and temperatures under study) is an unavoidable requirement for the correct behavior of the hybrid scheme.

The rest of the paper proceeds as follows. The equations governing the continuum and particle regions and the averaging procedures are presented in Sec. II. The core of the scheme, describing the $C \rightarrow P$ coupling for momentum, energy, and mass fluxes, is presented in Sec. III. General requirements on the coarse-graining length and time scales are discussed in Sec. IV. The unsteady flows under which the scheme has been tested (decay of longitudinal and transversal waves) are presented in Sec. V, and in Sec. VI we discuss the results of these tests as far as the main hydrodynamic and thermodynamic variables are concerned. Finally, Sec. VII is devoted to conclusions.

II. OVERVIEW AND GEOMETRY OF THE HYBRID COUPLING SCHEME

The domain decomposition of the hybrid scheme is depicted in Fig. 1. Two regions need to be distinguished: the particle region P and the continuum region C. Region P is composed of an ensemble of particles interacting through prescribed interparticle potentials and evolving in time through Newtonian dynamics. In order to illustrate the coupling procedure, a Lennard-Jones (LJ) fluid will be considered. Within P, a number $N(t)$ of particles, located at $\mathbf{r} = \{\mathbf{r}_i\}$ (the subscript i denoting the ith particle) interacts through the LJ potential $\psi(r) = 4\epsilon^{-1}[(\sigma/r)^{12} - (\sigma/r)^6]$. Each particle has a mass m, velocity $\mathbf{v}_i$, and energy $\epsilon_i = \frac{1}{2} m v_i^2 + \Sigma_j \psi(r_{ij})$ ($\mathbf{r}_{ij} = \mathbf{r}_j - \mathbf{r}_i$). Their equations of motion,

$$\dot{\mathbf{r}}_i = \mathbf{v}_i , \tag{1}$$

$$m\dot{\mathbf{v}}_i = \mathbf{f}_i = \sum_{j=1}^{N} \frac{d\psi(r_{ij})}{dr_{ij}} \frac{\mathbf{r}_{ij}}{r_{ij}}, \tag{2}$$

are solved via standard MD at time steps $\Delta t_P \simeq 10^{-3}\tau$, where $\tau = (m\sigma^2/\epsilon)^{1/2}$ is the characteristic time of the LJ potential. Throughout the rest of the paper, all quantities will be expressed in reduced units of the LJ potential: τ ($=0.45 \times 10^{-13}$ s), σ ($=3.305 \times 10^{-12}$ cm), ϵ, m ($=6.63 \times 10^{-23}$ g), and ϵ/k_B ($=119.18$ K) for time, length, energy, mass, and temperature, respectively (the numerical values correspond to argon).

On the other hand, within the C region the relevant variables are the macroscopic local densities associated with the conserved quantities, the number density $\rho(\mathbf{R},t)$, the energy density $\rho e(\mathbf{R},t)$, and the momentum density $\mathbf{j}(\mathbf{R},t)$ (related to the local mean velocity $\mathbf{u}$ by $\mathbf{j} = \rho\mathbf{u}$). In what follows, the spatial coordinates of the macroscopic fields are denoted by capital letters $\mathbf{R}$, while the the microscopic coordinates are designated by lowercase letters. The conservation laws for the local densities are

$$\frac{\partial \rho}{\partial t} = -\nabla \cdot \rho\mathbf{u}, \tag{3}$$

$$\frac{\partial \mathbf{j}}{\partial t} = -\nabla \cdot (\mathbf{ju} + \mathbf{\Pi}), \tag{4}$$

$$\frac{\partial \rho e}{\partial t} = -\nabla \cdot (\rho e\mathbf{u} + \mathbf{\Pi} \cdot \mathbf{u} + \mathbf{q}), \tag{5}$$

where the specific energy $e = u^2/2 + 3T/2 + \phi$ includes the translational energy, the thermal kinetic energy, and the potential energy ϕ. The momentum flow contains contributions from convection $\mathbf{ju}$ and the pressure tensor $\mathbf{\Pi} = P\,\mathbf{1} + \boldsymbol{\tau}$, the latter including the local hydrostatic pressure $P(\mathbf{R},t)$ and the

viscous stress tensor, which satisfy a Newtonian constitutive relation, as shown by previous MD descriptions of the LJ fluid [7,13];

$$\boldsymbol{\tau} = -\eta\left(\nabla\mathbf{u} + (\nabla\mathbf{u})^T - \frac{2}{3}\nabla\cdot\mathbf{u}\right) - \xi\nabla\cdot\mathbf{u}. \tag{6}$$

The energy current includes convection $\rho e\mathbf{u}$, dissipation $\boldsymbol{\Pi}\cdot\mathbf{u}$ and conduction $\mathbf{q}$, which can be expressed in terms of the local temperature gradients and the thermal conductivity κ_c, through Fourier's law $\mathbf{q} = -\kappa_c\nabla T(\mathbf{R},t)$. In order to close the above equations, it is necessary to know the caloric $e(\rho,T)$ and thermal equations of state $P(\rho,T)$, and the constitutive relations for the transport coefficients (shear and bulk viscosities and thermal conductivity; η, ξ, and κ_c, respectively) in terms of a set of independent thermodynamic variables, such as ρ and T. The equations of state for a LJ fluid were extracted from Johnson *et al.* [6] and the transport coefficients η, κ_c, and ξ from Heyes [7] and Borgelt *et al.* [8]. The variables relevant to the C region are the slower ones. Using any standard continuum fluid dynamics solver (e.g., based on a finite volume method), the evolution of the C variables will be traced at time intervals $\Delta t_C \gg \Delta t_P$ and evaluated within cells of volume V_l whose size and location are given by the nodes of a certain mesh, $\{\mathbf{R}_l\}$, $l = \{1,\ldots,M_c\}$. It will be assumed that the size of the $C \rightarrow P$ and $P \rightarrow C$ regions are the same size as those of the cells used in the spatial discretization of the selected continuum solver, say, $V_l = (\Delta X)^3$. In general, both ΔX and Δt_C may depend on the type of solver used for the C region, or on the characteristic length of the particular phenomena under study. Nevertheless, various intrinsic constraints on ΔX and Δt_C will be mentioned in Sec. IV.

Averages

Averages are needed in order to transfer information from the faster time-scale and shorter length-scale particle dynamics to the slower and longer coarse-grained description. In order to deal with unsteady, nonequilibrium scenarios, averages need to be local on the slower time scale and in the coarse-grained spatial coordinates. For any particle variable, say Φ_i, we define the following averages:

$$\overline{\Phi}(\mathbf{R}_l,t) \equiv \frac{1}{N_l}\sum_{i\in V_l}^{N_l}\Phi_i, \tag{7}$$

$$\langle\overline{\Phi}\rangle(\mathbf{R}_l,t_C) \equiv \frac{1}{\Delta t_C}\int_{t_C}^{t_C+\Delta t_C}\overline{\Phi}(\mathbf{R}_l,t)dt, \tag{8}$$

where the summation in Eq. (7) is made over the N_l particles inside the cell l.

The averaging procedure is needed to translate the P and C ''languages'' to and from each domain. This translation is done within the overlapping region, where the two descriptions of matter coexist (see Fig. 1). In particular, within the $P \rightarrow C$ cells, the many degrees of freedom arising from the particle dynamics are coarse grained to provide boundary conditions at the ''upper'' C-level. As long as the number of degrees of freedom is very much larger at P than at C, this operation is rather straightforward and is based on the microscopic derivation of continuum fluid dynamics [9]. We adopt the approach advocated by Flekkoy *et al.* [5], in making the information transferred from P to C to be the coarse-grained particle fluxes of conserved quantities. These are

$$\rho\mathbf{u}\cdot\mathbf{n}_{PC} = \frac{1}{V_{PC}}\left\langle\sum_{i=1}^{N_{PC}} m\mathbf{v}_i\right\rangle\cdot\mathbf{n}_{PC}, \tag{9}$$

$$\boldsymbol{\Pi}\cdot\mathbf{n}_{PC} = \frac{1}{V_{PC}}\left\langle\left(\sum_{i=1}^{N_{PC}} m\mathbf{v}_i\mathbf{v}_i - \frac{1}{2}\sum_{i,j}^{N_{PC}}\mathbf{r}_{ij}\mathbf{F}_{ij}\right)\right\rangle\cdot\mathbf{n}_{PC}, \tag{10}$$

$$\mathbf{q}\cdot\mathbf{n}_{PC} = \frac{1}{V_{PC}}\left\langle\left(\sum_{i=1}^{N_{PC}} m\boldsymbol{\epsilon}_i\mathbf{v}_i - \frac{1}{2}\sum_{i,j}^{N_{PC}}\mathbf{r}_{ij}\mathbf{v}_i\mathbf{F}_{ij}\right)\right\rangle\cdot\mathbf{n}_{PC}, \tag{11}$$

where N_{PC} is the number of particles inside the $P \rightarrow C$ cell and $\mathbf{n}_{PC}$ is the surface vector shown in Fig. 1.

By contrast, within the $C \rightarrow P$ cells, the particle dynamics must be modified to conform to the averaged-dynamics prescribed by the continuum description. In other words, one needs to construct a sort of ''generalized boundary condition'' for the particle dynamics. As pointed out in all previous papers on the subject [1–3,5], this represents the most demanding challenge in that one needs to *invent* a way to reconstruct the microscopic dynamics of a large number of particles, based on only a few properties of the local continuum variables. Moreover, to ensure that the effect on the inner P region is minimized, it is crucial to reduce as much as possible the unphysical artifacts, such as Maxwell demons, which are added to the particle dynamics at $C \rightarrow P$. The present work is focused on this problem, which lies at the core of any hybrid scheme.

III. THE $C \rightarrow P$ COUPLING

This part of the hybrid scheme can be alternatively stated as the imposition of generalized (mass, momentum, and energy) boundary conditions on an MD simulation box. To deal with this task we have coupled the particle region to a collection of flows (with explicit analytical solution), which involves the whole set of conserved quantities exchanged (mass, momentum, and energy). In this sense, in the present work our C-solver is not numerical but rather analytical. In particular, we use the initial (nonequilibrium) state imposed at P to calculate the time-dependent analytical solution at C. This C-flow is then imposed on the P region during the rest of the simulation, meaning that (appart from the initial state) the hybrid coupling used in the tests presented here works in one direction only (from C to P).

A. Imposing fluxes under unsteady flows

Following Flekkoy *et al.* [5], at $C \rightarrow P$ we shall communicate fluxes of conserved quantities. These fluxes correspond to mass, momentum, and energy transfers through the outer interface of the $C \rightarrow P$ cell (the W surface in Fig. 1).

Flekkoy *et al.* [5] obtained these fluxes from the values of the continuum variables at the center of the control cell, $x = x_O$, instead of at the exact position of the $C \rightarrow P$ interface, $x = x_W$. We have found that it is essential to take into account this apparently unimportant technicality when dealing with unsteady scenarios. Let us consider a general conservation equation, with

$$\frac{\partial \phi}{\partial t} + \nabla \cdot \mathbf{J}_\phi = S_\phi, \tag{12}$$

where J_ϕ is the flux of ϕ and the source term vanishes, $S_\phi = 0$, as in Eqs. (3)–(5). Integrating over the control cell $C \rightarrow P$,

$$\frac{\partial}{\partial t}\int_V \phi dV + \int_S \mathbf{J}_{\boldsymbol{\phi}} \cdot \mathbf{n} ds = 0. \tag{13}$$

For illustration, we shall restrict analysis to the one-dimensional (1D) situation depicted in Fig. 1. In this case one obtains

$$\frac{\partial}{\partial t}\int_V \phi dV - A\mathbf{J}_{\phi E} \cdot \mathbf{n}_W = -A\mathbf{J}_{\phi W} \cdot \mathbf{n}_W, \tag{14}$$

where the subscripts E (east) and W (west) denote that the variables are measured at $x = x_E$ and $x = x_W$, respectively. The surface vectors $\mathbf{n}_W$ and $\mathbf{n}_E$ are shown in Fig. 1, and in Eq. (14) use has been made of $\mathbf{n}_W = -\mathbf{n}_E$. The right-hand side (RHS) of Eq. (14) is the flux current of ϕ through the interface W of the control cell, which is precisely the (generalized) force we want to introduce on the particles at the $C \rightarrow P$ buffer. We note that only under steady flows does $\mathbf{J}_{\phi W} = \mathbf{J}_{\phi O}$ (to see this, integrate Eq. (12) from $x = x_O$ to $x = x_W$). Hence only in this case does the evaluation of the fluxes at x_W using the continuum variables at x_O lead to the same converged steady state as if the variables at x_W were used (although the transients may of course differ). It is possible to provide an estimate of the global error arising from evaluating the flux at a position x_O shifted $\delta \Delta X$ with respect x_W, over a certain time interval Δt. In the case of the momentum equation, the deviation of the stress contribution to the momentum flux $J = \mathbf{J} \cdot \mathbf{n}$ at any instant would be of order $\Delta J \simeq \nabla J \, \delta \Delta X$, with $\delta = |x_O - x_W|/\Delta X$ being the distance to the $C \rightarrow P$ interface ($\delta = 0.5$ in Fig. 1). Assuming that the mean velocity field can be expressed as $u = \mathbf{u} \cdot \mathbf{n} \sim u^{(k)} \exp(ikx)$ (k being the dominant wave number) and using the Newtonian constitutive relation for the viscous tensor in Eq. (6), one obtains $\Delta J \sim \eta_L k^2 u^{(k)} \delta \Delta X$, where $\eta_L = 4\eta/3 + \xi$ is the longitudinal viscosity. As a particular example, we consider a longitudinal wave and evaluate the error along a cycle, $\Delta t = 2\pi/(kc_s)$ (where c_s is the sound velocity). As a crude estimate, the accumulated error of the cell-averaged momentum $\mathbf{j} \cdot \mathbf{n} = \rho_e \overline{u}$ is of order $\rho_e \Delta \overline{u} \sim \Delta J \Delta t / \Delta X$; using $\rho_e = 0.5$, $\eta_L \simeq 1$, and $c_s \simeq 5$, one obtains $\Delta \overline{u}/u^{(k)} \sim 2\pi \delta \eta_L k/(c_s \rho_e) \simeq 0.3$ for the typical wave numbers considered here ($k \sim 0.2$). Simulations carried out with the momentum flux evaluated at x_O yield relative errors of the averaged velocity at $C \rightarrow P$ of the same order of magnitude as this estimate [see Sec. VI C 2 and Fig. 6(b)]. We observe that most CFD codes provide the continuum variables at the center of the control cells (i.e., at x_O), so that in order to evaluate the fluxes pertaining to the $C \rightarrow P$ exchange it would first be necessary to make use of simple interpolation techniques.

The fluxes arising from the continuum equations [on the RHS of Eqs. (15)–(17)] are imposed on the particle ensemble at the $C \rightarrow P$ cells through expressions involving atomistic variables [those on the LHS of Eqs. (15)–(17)].

$$ms = -A\rho \mathbf{u} \cdot \mathbf{n}, \tag{15}$$

$$ms\langle \mathbf{v}' \rangle + \left\langle \sum_i^{N_{CP}} \mathbf{F}_i^{ext} \right\rangle = -A(\rho \mathbf{uu} + \boldsymbol{\Pi}) \cdot \mathbf{n}, \tag{16}$$

$$ms\langle \boldsymbol{\epsilon}' \rangle + \left\langle \sum_i^{N_{CP}} \mathbf{F}_i^{ext} \cdot \mathbf{v}_i \right\rangle - \langle \mathbf{J}_Q^{ext} \rangle \cdot \mathbf{n} = -A(\rho \mathbf{u} e + \boldsymbol{\Pi} \cdot \mathbf{u} + \mathbf{q}) \cdot \mathbf{n}, \tag{17}$$

where henceforth, $\mathbf{n}$ indicates the vector of the outermost interface of the $C \rightarrow P$ cell, pointing towards C. The nomenclature used here follows that of Flekkoy *et al.* [5]: $s(t)$ indicates the number of particles inserted ($s > 0$) or removed ($s < 0$) from $C \rightarrow P$ per unit of time; the velocity of the inserted or removed particles is $\mathbf{v}'$; $\mathbf{F}_i^{ext}$ is the external force applied to each particle i within the $C \rightarrow P$ cell. The total external force is $\Sigma^{N_{CP}} \mathbf{F}_i^{ext}$, where the summation is over the $N_{CP}(t)$ particles inside $C \rightarrow P$. Finally, $\langle \boldsymbol{\epsilon}' \rangle$ indicates the energy of the inserted or removed particles and $\langle \mathbf{J}_Q^{ext} \rangle$ refers to an externally imposed heat current.

As mentioned by Flekkoy *et al.* [5], insertion of Eq. (15) into Eq. (16) shows that the rates of change of momentum due to convection and local stresses are correctly introduced if $\langle \mathbf{v}' \rangle = \mathbf{u}$ and $\langle \Sigma_i^{N_{CP}} \mathbf{F}_i^{ext} \rangle = -A\,\boldsymbol{\Pi} \cdot \mathbf{n} = -A(P\mathbf{n} + \boldsymbol{\tau} \cdot \mathbf{n})$, respectively. Note that $-P\mathbf{n}$ is the hydrostatic pressure force (pointing inwards the $C \rightarrow P$ cell), while the viscous contribution $-\boldsymbol{\tau} \cdot \mathbf{n}$ depends on the local velocity gradient.

The balance of the energy flux requires some extra conditions. In Eq. (17) the convection, dissipation, and conduction of energy are balanced if $\langle \boldsymbol{\epsilon}' \rangle = e$, $\langle \Sigma_i^N \mathbf{F}_i^{ext} \cdot \mathbf{v}_i \rangle = -A\boldsymbol{\Pi} \cdot \mathbf{u} \cdot \mathbf{n}$ and $\langle \mathbf{J}_Q^{ext} \cdot \mathbf{n} \rangle = A\,\mathbf{q} \cdot \mathbf{n}$, respectively.

Let us now consider in more detail how the scheme deals with momentum, energy, and mass transfer from C to P.

B. Momentum exchange

The condition $\langle \mathbf{v}' \rangle = \mathbf{u}$ ensures the balance of momentum convection. If the mass flux points towards the P region ($s > 0$), this condition is fulfilled by choosing the velocity of the inserted particles from a Maxwellian distribution according to the local temperature at the $C \rightarrow P$ cell, $P(\mathbf{v}') = (1/2\pi mkT)^{3/2} \exp[-m(\mathbf{v}' - \mathbf{u})^2/2mkT]$. Concerning particle removal ($s < 0$), we note that if the average velocity at the $C \rightarrow P$ cell is equal to the continuum velocity $\langle \overline{\mathbf{v}} \rangle = \mathbf{u}$, then the average velocity of the subset of extracted particles

would be precisely $\langle \mathbf{v}' \rangle = \langle \overline{\mathbf{v}} \rangle = \mathbf{u}$. Hence the condition of velocity continuity at $C \to P$ is needed to ensure the correct balance of momentum convection.

The change of momentum due to local stresses establishes the overall external force exerted on the particle region. Therefore one needs to determine how the overall external force is distributed on each individual particle. Flekkoy *et al.* [5] distributed the force according to a certain function $g(x)$ satisfying $g(x_W) = \infty$, $g(x_O) = g'(x_O) = 0$. Normalization leads to

$$\mathbf{F}_i^{ext} = -\left(\frac{g(x_i)}{\sum_i^{N_{CP}} g(x_i)} \right) A \boldsymbol{\Pi} \cdot \mathbf{n}, \tag{18}$$

where x runs perpendicular to the $C \to P$ interface and the applied force is made constant along each Δt_C. As $g(x)$ tends to infinity as $x \to x_W$, the applied force diverges as one approaches the $C \to P$ interface; hence the density nearby $x = x_W$ is very small or zero. The function $g(x)$ is thus endowed with a twofold purpose: it ensures a limiting extension to P (as the hydrostatic pressure force always points towards the P region, particles will never cross the $C \to P$ interface outwards) while also guaranteeing the existence of a small region where particles can be inserted with very low risk of overlapping.

Despite the benefits of the $g(x)$ function for distributing the externally imposed momentum, we decided to use $g(x) = 1$ for all x inside the $C \to P$ cell. The reasons for this choice will become clear when explaining the energy exchange, below. The first implication of $g(x) = 1$ is that the external force is equally distributed among all the particles within the $C \to P$ cell. In other words, $\mathbf{F}_i^{ext}$ no longer depends on the particle label,

$$\mathbf{F}_i^{ext} = \mathbf{F}^{ext} = -\left(\frac{1}{N_{CP}} \right) A \boldsymbol{\Pi} \cdot \mathbf{n}. \tag{19}$$

The second implication of $g(x) = 1$ is that the particle density profile near the $C \to P$ interface no longer vanishes, so one needs an efficient way to resolve the problem of overlap on the insertion of new particles. This task is carried out by the USHER algorithm, as explained below. Finally, in order to ensure a finite extent of the particle region, if a particle (i) crosses outwards the $C \to P$ interface (in Fig. 1, $x_i = x_W - \delta$, with $\delta > 0$) with velocity $\mathbf{v}_i$, it is substituted by another one (j) with $y_j = y_i$; $z_j = z_i$, $x_j = x_W + \delta$, and with $\mathbf{v}_j = \mathbf{v}_i$. In this way, the overall momentum is strictly conserved before and after the particle exchange.

C. Energy exchange

1. Advection

The balance of advected energy requires that $\langle \epsilon' \rangle = e = u^2/2 + 3T/2 + \phi$. Decomposing the particle energy into the kinetic and potential parts, $\epsilon' = (v')^2/2 + \psi'$, one sees that since the new particles are drawn from a Maxwell distribution, therefore $\langle (v')^2/2 \rangle = u^2/2 + 3T/2$. By contrast, the balance of potential energy $\langle \psi' \rangle = \phi$ is much less straightforward to implement. This condition is fulfilled by the USHER algorithm, described below.

2. Dissipation

One needs to satisfy the following balance of heat dissipation:

$$\left\langle \sum_i^{N_{CP}} \mathbf{F}_i^{ext} \cdot \mathbf{v}_i \right\rangle = -A \boldsymbol{\Pi} \cdot \mathbf{u} \cdot \mathbf{n}. \tag{20}$$

This condition does not generally hold if the external force is distributed according to an arbitrary $g(x)$. Indeed, it is not even clear that a function $g(x)$ exists satisfying $g(x_W) \to \infty$ and enabling the heat dissipation balance in Eq. (20). In any case, such a function g would depend on the particle's velocity distribution, and then the problem of finding g would become a formidable task at each time step.

The advantage of using $g(x) = 1$ now becomes clear. As long as $\mathbf{F}_i^{ext}$ does not depend on the particle label, one can greatly simplify the left-hand side of Eq. (20) to obtain

$$\mathbf{F}^{ext} \cdot \left\langle \sum_i^{N_{CP}} \mathbf{v}_i \right\rangle = N_{CP} \mathbf{F}^{ext} \cdot \langle \overline{\mathbf{v}} \rangle = -A \boldsymbol{\Pi} \cdot \mathbf{u} \cdot \mathbf{n}. \tag{21}$$

The last equality follows from construction of the overall force $N_{CP} \mathbf{F}^{ext} = -A \boldsymbol{\Pi} \cdot \mathbf{n}$, and from the continuity of velocity $\langle \overline{\mathbf{v}} \rangle = \mathbf{u}$.

3. Conduction

The condition $\langle \mathbf{J}_Q^{ext} \rangle \cdot \mathbf{n} = A \mathbf{q} \cdot \mathbf{n}$ requires the establishment of a heat current along the $C \to P$ cell representing the conduction of energy. This may be implemented by various means; for instance, following the idea of Evans and Morris [9] one may include an extra force that pulls the ''hotter'' particles towards the direction of the heat flux and conserves the overall momentum. Alternatively, one may try to impose a Chapman-Enskog velocity distribution with the desired heat flux, at some region inside the $C \to P$ buffer. In this work we have made use of the phenomenological Fourier's law, $\mathbf{q} = -\kappa_c \nabla T$. A temperature gradient is imposed along each $C \to P$ cell by using a set of Nosé-Hoover thermostats (NHT's) placed along the direction of the heat flux. The outer and inner thermostats are located a distance d apart, and the temperature difference between both set to $d \nabla T \cdot \mathbf{n}$. Typically, at each $C \to P$ cell we have used a set of two or three NHT's along a distance of 3σ or 4σ. The values of the Q parameter appearing in the NHT formulation [10] were chosen small enough to minimize unphysical dynamics, i.e., we have chosen $Q \simeq 5$. The main benefit of using the Nosé-Hoover formulation is the small distortion these thermostats introduce to the particle dynamics compared with other ways of implementing thermostatting [10].

D. Mass exchange: Particle insertion

One important condition on the particle insertion, inherited from the balance of potential energy, is $\langle \psi' \rangle = \phi$ (see

Sec. III C). To deal with this task, our strategy has been to place the new particles in positions where $\psi' \simeq \phi$. As ϕ is, roughly speaking, the energy needed to insert a new particle, we shall insert particles with energies close to the local chemical potential. In any case, this implies that the insertions need to be made in very precise positions which depend on the configuration of the rest of the particles. To this end we have developed an algorithm (USHER) that guides each new inserted particle to a position where the potential energy is equal to ϕ (up to a prespecified threshold). A brief explanation is given below (see the work of Delgado-Buscalioni and Coveney [11] for further details). We first note that while the USHER algorithm guides a new particle to a correct location, the rest of the particles remain frozen in position. USHER essentially performs the following steps:

(1) Place the new particle ($i=N+1$) at an initial position inside $C \rightarrow P$, $\mathbf{r}^{(0)}$.

(2) Evaluate $\mathbf{f}_{N+1}=\Sigma_{j=1}^{N}\mathbf{f}_{N+1,j}$ and

$$\delta t_\sigma = \sqrt{\frac{2\,\delta r}{|\mathbf{f}_{N+1}|}}.$$

Typically one can use $\delta r \simeq \sigma$.

(3) Move the new particle according to the update rule

$$\mathbf{r}^{(n+1)} = \mathbf{r}^{(n)} + \frac{1}{2}\mathbf{f}_{N+1}^{(n)}\delta t^2,$$

where $\delta t = \min(\Delta_t, \delta t_\sigma)$, with $\Delta_t \simeq 0.05$ in reduced units.

(4) Evaluate the relative difference between the specific internal energy of the new particle, ψ'_{N+1}, and that prescribed by the continuum, ϕ: $R_{Err}=|\psi'_{N+1}-\phi|/|\phi|$.

(5) The particle is correctly inserted if R_{Err} is small enough (typically ~ 0.1).

Let us show how the USHER algorithm easily overcomes the problem of possible initial overlap with preexisting particles. An overlap leads to very large values of the interparticle force, $f_{N+1} \gg 1$, so in this case $\delta t_\sigma \ll 1$ and $\delta t = \delta t_\sigma$. But by construction, during the interval δt_σ, the new particle moves a distance of the order of the particle size σ in the direction of minimum energy, just enough to avoid any initial overlap. Then, as the particle steadily moves towards a local minimum of energy, f_{N+1} decreases, and δt_σ increases until it becomes larger than Δ_t. Then, $\delta t = \Delta_t$ is fixed. For liquid densities varying between $\rho=0.5$ and -0.8, the USHER algorithm typically needs 15–90 iterations (single-force evaluations) to correctly place a new particle [12]. By introducing the particles with $\psi' = \phi(1 \pm R_{Err})$, we found that, upon averaging over Δt_C, the condition $\langle \psi' \rangle = \phi$ holds within about 2% (even using values of R_{Err} as large as 0.5).

Until now we have not mentioned any limitation on the sizes of the coarse mesh and time step, ΔX and δt_C. Comments on this topic are very scarce in the previous literature on hybrid methods for fluids. Moreover, since the local averages are made using these spatial and temporal windows, it is also appropriate to formulate any condition on ΔX and Δt_C before presenting the results of the tests carried out for different flows.

IV. LENGTH AND TIME-SCALE PREREQUISITES

A. Arising from consideration of the microscopic description

Continuum fluid dynamics rest on the local equilibrium assumption. This means that, in order to define a local thermodynamic and hydrodynamic state characterizing the coarse-grained variables at the $C \rightarrow P$ and $P \rightarrow C$ cells, the size of these cells needs to be greater than the mean free path λ extracted from the particle dynamics. Moreover, the local equilibrium within each cell should be attained on time scales smaller than Δt_C. This means that Δt_C has to be larger than the collision time τ_{col}. In summary, $\Delta X > \lambda$ and $\Delta t_C > \tau_{col}$. In the case of a LJ fluid, it is possible to use the hard-sphere approximation to make an order-of-magnitude estimate, $\Delta X > 0.2\rho^{-1}$ and $\Delta t > 0.14\rho^{-1}T^{-1/2}$. These conditions become less restrictive at larger densities; as an example, for $T=1$, $\rho=0.5$, and a typical MD time step $\Delta t_P \sim 10^{-3}$, local equilibrium would require $\Delta t_C/\Delta t_P \geqslant 100$ integration steps.

B. Arising from consideration of the hydrodynamic description

Conditions on ΔX and Δt_C are firstly imposed by the smallest characteristic length and time scales involved in the process under investigation (say, $2\pi/k_{\max}$ and $2\pi/\omega_{\max}$, respectively). Practically, to correctly recover the smallest spatio temporal flow pattern, one needs at least eight points per period, so $\Delta t_C \leqslant \pi/4\omega_{\max}$ and $\Delta X \leqslant \pi/4k_{\max}$. The numerical stability of the *C*-solver algorithm may also impose limitations. As mentioned in Sec. I, algorithms with explicit time discretization are better suited for the *C* solver of a hybrid scheme. A necessary condition for their numerical stability is $C = U\Delta t_C/\Delta X \leqslant 1/2$, where *C* is the Courant number and *U* the maximum characteristic flow velocity. The value of *U* depends on the physical process one is dealing with, but, to provide numbers in the present discussion, let us assume that we are dealing with low or moderate Reynolds numbers. Then, if the process is a diffusive one, $U=\nu/\Delta X$; alternatively, if sound waves are relevant within the flow, $U=c_s$. In summary, the computational window for Δt_C should be $0.14\rho^{-1}T^{-1/2} < \Delta t_C \leqslant \Delta X/(2U)$. Using the maximum grid spacing allowed, $\Delta X = \pi/4k_{\max}$, one obtains the computational windows for Δt_C shown in Fig. 2 versus ρ, for $k_{\max}=\{0.1,0.2\}$, $U=\{\nu/\Delta X, c_s\}$, and $T=2.5$. As expected, a sound wave requires smaller time steps than a diffusive process. For large enough $k_{\max}$, the temporal and spatial computational window may be highly localized; e.g., for $\rho=0.5$, one should use $0.2 < \Delta t_C < 0.5$ if waves with wavelengths smaller than 30σ need to be captured by the coarse-grained description. As the density decreases, these conditions become much more restrictive, until the acoustic time finally becomes smaller than the collision time (see Fig. 2). Also, in rarefied gases, if $\rho < k_{max}/4$, the mean free path becomes larger than the wavelength, but here we shall not be concerned with situations where the Navier-Stokes equations are not appropriate (see Garcia *et al.* for further discussion [1]).

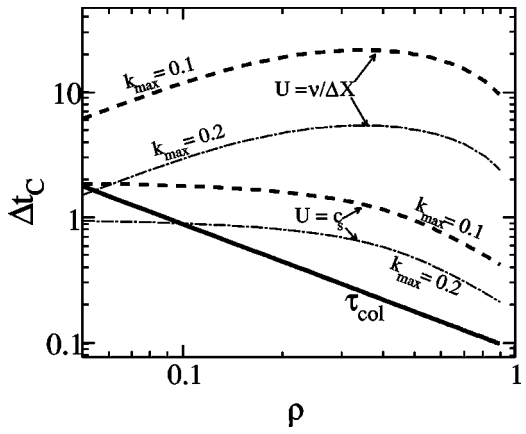

FIG. 2. Conditions imposed on the time step of the continuum solver Δt_C plotted versus the number density ρ. Variables are expressed in the LJ reduced units [σ for length and $\tau=(\sigma^2 m/\epsilon)^{1/2}$ for time]. As discussed in Sec. IV B, Δt_C has to be greater than the collision time τ_{col} (the thick solid line) and smaller than $\Delta X/(2U)$ (indicated with dashed and dash-dotted lines). The typical flow velocity U is chosen to be either the sound velocity $U=c_s$ or the diffusive velocity $U=\nu/L$, according to each case discussed in Sec. IV B. The grid spacing is $\Delta X=\pi/(4k_{\max})$, where $k_{\max}$ is the largest wave number to be captured within the flow.

V. TESTS: HYDRODYNAMIC MODES

As already mentioned, our hybrid scheme has been tested under stationary and unsteady flows. Typical stationary nonequilibrium states were considered, such as heat conduction profiles [13] and Couette profiles [5,13]. The microscopic reconstruction of these flows has been so well studied in the literature that nothing new may added here. In passing, we note that the transient times to achieve the steady state from the rest solution were found to be in agreement with the diffusive times L_x/κ and L_x/ν. The rest of the discussion will be focused on our choice of unsteady scenarios, which are described by the decay of transversal and longitudinal waves. These flows are now briefly presented, using standard hydrodynamics.

Consider a fluid at equilibrium characterized by homogeneous mass density ρ^e, specific energy e^e, and a vanishing mean velocity $\mathbf{u}^e=0$. Our procedure is to perturb this equilibrium state with different hydrodynamic fields $\{\rho^p,\mathbf{u},e^p\}$ (periodic in the x direction, i.e., $\mathbf{k}=k\mathbf{i}$) and then make use of the $C\rightarrow P$ coupling scheme described in Sec. III to verify that, within the particle region, the subsequent evolution towards equilibrium is carried out in a hydrodynamically consistent way. If use is to be made of the linear hydrodynamic theory, the externally induced perturbations should be small enough to guarantee that the relaxation process is always governed by the linearized mass, momentum, and energy equations (3)–(5) [14]. We defer further discussion of this point to Sec. VI below.

As is customary, to solve the linearized set of equations, a Laplace-Fourier transform (LFT) is first performed [14]. The LFT of any perturbative variable, say $\Phi(\mathbf{r},t)$, will be denoted as

$$\Phi(\mathbf{k},t)\equiv\int_{-\infty}^{\infty}\Phi(\mathbf{r},t)\exp(-i\mathbf{k}\cdot\mathbf{r})d\mathbf{r}, \tag{22}$$

$$\hat{\Phi}(\mathbf{k},z)\equiv\int_{0}^{\infty}dz\,\exp(izt)\Phi(\mathbf{k},t)dt. \tag{23}$$

The LFT of the linearized equation [Eqs. (3)–(5)] leads to the following algebraic system for $\hat{\mathbf{\Phi}}=(\hat{\rho}^p,\hat{T}^p,\hat{j}_x^p,\hat{j}_y^p,\hat{j}_z^p)$ [14],

$$\mathbf{M}\hat{\mathbf{\Phi}}^T(\mathbf{k},z)=\mathbf{\Phi}^T(\mathbf{k},0), \tag{24}$$

where the hydrodynamic matrix is

$$\mathbf{M}=\begin{pmatrix} -iz & 0 & ik & 0 & 0 \\ 0 & -iz+\kappa\gamma k^2 & ik\dfrac{\gamma-1}{\rho^e\alpha} & 0 & 0 \\ ikc_s^2/\gamma & ikD & -iz+bk^2 & 0 & 0 \\ 0 & 0 & 0 & -iz+\nu k^2 & 0 \\ 0 & 0 & 0 & 0 & -iz+\nu k^2 \end{pmatrix}. \tag{25}$$

We note that instead of using e^p, the energy equation is expressed in terms of temperature fluctuations. Also, for clarity, it is better to write the solution $\hat{\mathbf{\Phi}}$ in terms of the $t=0$ Fourier-transformed perturbative heat density Q^p and pressure P^p. These quantities are related to ρ^p and T^p through the relations

$$e^p=c_v T^p+\left(\frac{\partial e}{\partial\rho}\right)_{T^e}\rho^p, \tag{26}$$

$$Q^p=\rho^e c_v\left(T^p-\frac{\gamma-1}{\rho^e\alpha}\rho^p\right), \tag{27}$$

$$P^p = \frac{mc_s^2}{\gamma}(\rho^e \alpha T^p - \rho^p). \tag{28}$$

Here c_p and c_v are the specific heats at constant pressure and volume, respectively; $\gamma = c_p/c_v$ is the adiabatic coefficient; $\kappa = \kappa_c/c_p\rho^e$ is the thermal diffusivity; $\alpha = -(\partial\rho/\partial T)_P/\rho^e$ the thermal expansion coefficient; and the kinematic longitudinal viscosity $b = (4\eta/3 + \xi)/\rho^e$ is related to the sound attenuation coefficient Γ through $2\Gamma = b + (\gamma - 1)\kappa$. Finally $D = (\partial P/\partial T)_\rho$ and the adiabatic speed of sound is $c_s^2 = \gamma(\partial P/\partial\rho)_T$.

Provided that, in the hydrodynamic limit, the wavelengths of the perturbations are much larger than the mean interparticle distance, it is sufficient to obtain the solution of Eq. (24) up to $O(k^2)$ [14]. Putting $z \to \omega \in \mathcal{R}$ into Eqs. (24) and (25) leads, after some algebra, to the following identities

$$\hat{T}(\mathbf{k},\omega) = \frac{E_\kappa Q(\mathbf{k},0)}{\rho^e c_p} + \frac{\gamma - 1}{\rho^e \alpha} E_{SR} P(\mathbf{k},0) + \frac{\gamma - 1}{\rho^e \alpha c_s} E_{SI} j_x(\mathbf{k},0), \tag{29}$$

$$\hat{\rho}(\mathbf{k},\omega) = -\frac{\alpha}{c_p} E_\kappa Q(\mathbf{k},0) + \frac{1}{mc_s^2} E_{SR} P(\mathbf{k},0) + \frac{1}{c_s} E_{SI} j_x(\mathbf{k},0), \tag{30}$$

$$\hat{j}_x(\mathbf{k},\omega) = \frac{1}{mc_s} E_{SI} P(\mathbf{k},0) + E_{SR} j_x(\mathbf{k},0), \tag{31}$$

$$\hat{j}_y(\mathbf{k},\omega) = E_\nu j_y(\mathbf{k},0), \tag{32}$$

$$\hat{j}_z(\mathbf{k},\omega) = E_\nu j_z(\mathbf{k},0), \tag{33}$$

and, using Eqs. (27) and (28),

$$\hat{Q}(\mathbf{k},\omega) = E_\kappa Q(\mathbf{k},0), \tag{34}$$

$$\hat{P}(\mathbf{k},\omega) = E_{SR} P(\mathbf{k},0) + mc_s E_{SI} j_x(\mathbf{k},0), \tag{35}$$

where the following propagators have been introduced,

$$E_\kappa(k,\omega) = \exp(-\kappa k^2 t), \tag{36}$$

$$E_{SR}(k,\omega) = \exp(-\Gamma k^2 t)\cos(c_s k t), \tag{37}$$

$$E_{SI}(k,\omega) = -i\exp(-\Gamma k^2 t)\sin(c_s k t), \tag{38}$$

$$E_\nu(k,\omega) = \exp(-\nu k^2 t). \tag{39}$$

The shear or transverse modes correspond to momentum perturbations along y and/or z axis (i.e., perpendicular to the wave vector $k\mathbf{i}$); from Eqs. (32) and (33), it is clear that they are completely decoupled. The remaining hydrodynamic variables $\{\rho^p, T^p, j_x^p\}$ are coupled and conform to three longitudinal modes that can be divided into two subgroups: two sound modes (involving longitudinal momentum and pressure at constant entropy) and one heat mode (involving heat diffusion). The fact that the heat density is an independent mode is evident from Eq. (34), where it is seen that it relaxes diffusively, being proportional to $\exp(-\kappa k^2 t)$. We note that $Q^p = T^e s^p$ is essentially the fluctuation of the entropy density s^p [14]. From Eqs. (31) and (35), it is easily shown that the two sound modes $(\hat{P}/c_s \pm \hat{j}_x)$ decay like $\exp(ikc_s t - \Gamma k^2 t)$.

VI. RESULTS

A. Setup and initial states

The coupling scheme was implemented and tested in the setup shown in Fig. 3. The system is periodic along y and z directions, and the gradients of the continuum variables are set along the x direction. The particle region occupies a region of size L_x around $x = 0$ and of size $L_y = L_z$ along the periodic directions. The P region is divided into control cells of size ΔX, wherein local averages are taken. The centers of the two $C \to P$ slabs (the outermost cells) are situated at $x = \pm|L_x - \Delta X/2|$. The deviation from the local equilibrium assumption was monitored in terms of the relative difference of the cell-averaged pressure and energy with respect the values given by the equation of state of Johnson *et al.*, Ref. [6]. Around a distance 1.5σ away from the $C \to P$ interface, the typical maximum deviations were only about 6%.

The initial perturbative flow was prepared by first letting the P region relax until a vanishing and homogeneous mean flow was obtained. Then, during a small time interval $(\sim 3\tau)$, the particle velocities were periodically changed according to a Maxwellian distribution with the desired velocity profile and local cell temperature. The resulting initial state was then analyzed to extract the Fourier components of the whole set of flow variables $(\mathbf{v}, \rho, T, e, P)$. For the sake of consistency these were extracted by Fourier transforms of the cell-averaged variables,

$$\overline{\phi}_{\cos}^{(n)}(t) \equiv \frac{c_n}{M_c} \sum_l^{M_c} \overline{\phi}(X_l, t)\cos(k_n X_l), \tag{40}$$

$$\overline{\phi}_{\sin}^{(n)}(t) \equiv \frac{c_n}{M_c} \sum_l^{M_c} \overline{\phi}(X_l, t)\sin(k_n X_l), \tag{41}$$

where $k_n = nk$ $(n \in \mathcal{N})$; and $c_n = 1$ for $n = 0$, and $c_n = 2$ otherwise. In any case, it was checked that the Fourier transform of the microscopic variables $\phi^{(n)} = c_n \Sigma_i^N \phi(x_i, t) \times \exp(-ik_n x_i)/N$ yields essentially the same output as Eqs. (40) and (41).

The initial Fourier transforms calculated from Eqs. (40) were injected into Eqs. (29)–(35) to obtain the time evolution of the continuum variables. These, in turn, were used to calculate the fluxes imposed on the $C \to P$ cells over time. The transport coefficients used were those reported in the literature [7,6]. As an interesting check, it was found that the coupling scheme failed significantly if the transport coefficients used in the C region differed by more than about 15% from those of the LJ fluid. In particular, the oscillation frequency of the averaged particle velocity differed with respect to that of C, while correlations decayed at a faster rate than those of the C flow. Therefore, in cases where the constitutive relations are not known, this result means that it is first necessary to measure the transport coefficients from the par-

ticle dynamics (using any standard molecular technique), before applying the hybrid scheme, particularly if unsteady flows are to be studied.

The wavelengths of the initial perturbations were chosen to be much larger than the mean free path (i.e., $2\pi\lambda/k \ll 1$), in order to work within the hydrodynamic regime. In other words, the dependence of the transport coefficients on the wavenumber was negligible [14]. The amplitudes of the initial perturbation were chosen small enough to ensure that the subsequent relaxation process could be described by the linear theory. In particular, if $\overline{\mathbf{v}}^{(1)}(t)$ is the maximum Fourier amplitude of the velocity, the typical values of the Reynolds number at $t=0$ $[\mathrm{Re}=|\overline{\mathbf{v}}^{(1)}|\rho_e/(k\eta)]$ were $\mathrm{Re}(0)\leqslant 3$. As $|\overline{\mathbf{v}}^{(1)}(t)|$ decays exponentially, convection was present only in the first stages of the relaxing flow, but it was not strong enough to produce significant deviations from the linear theory (nonlinear effects become dominant for $\mathrm{Re}>O(10)$ [15]). The maximum Mach number was less than 0.2, and density fluctuations were around $|\overline{\rho}^{(1)}|/\rho_e \sim \mathrm{Ma}^2 \simeq 0.05$.

In another test, the hybrid scheme was applied to a fluid in mechanical ($\mathbf{u}=0$) and thermodynamical equilibrium ($\rho=0.5$, $T=3.5$, $e=2.7$, $P=3.2$) during a longer simulation (50τ) to check for any possible spurious drift in the overall momentum and energy [note that Eq. (15) ensures the mass conservation by construction]. During this calculation, the total momentum inside the P region was conserved up to 5×10^{-4}, and the total energy fluctuated $\sim 5\%$ around its equilibrium value. The size of these fluctuations is consistent with the system size (which contained $N=1600$ particles and a specific heat of $c_v=1.8$). Note that the total energy of the system cannot be conserved because a part of the system is connected to a thermostat, and it also receives mechanical energy from C.

B. Transversal waves

In order to test the transfer of momentum flux along the direction perpendicular to the $C\rightarrow P$ interface, planar shear waves along x were excited in a LJ fluid with $\rho=0.5$, $T=2.5$, and $\eta=0.75\pm0.05$ (the error bar comes from Ref. [7]). These waves were created by imposing sinusoidal y-velocity profiles $v_y(x)=v^{(1)}_{y,\mathrm{sin}}\sin(kx)$.

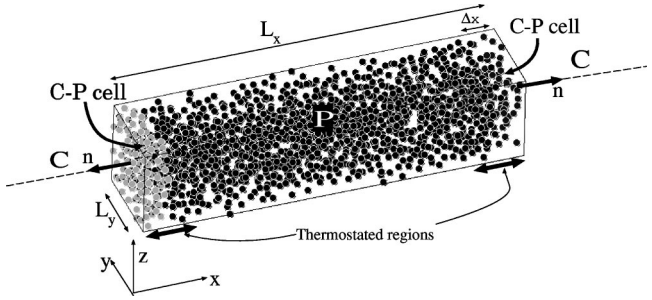

FIG. 3. The setup for which the scheme has been tested (here region P is surrounded by C). The fluxes of continuum variables are imposed along the x direction, while y and z are periodic. The hybrid coupling is applied at the $C\rightarrow P$ cells and the heat current is established along the Nosé-Hoover thermostatted regions whose thickness is set between $(3-4)\sigma$. We used $\Delta X=(1-2)\sigma$, $L_x=(10-40)\sigma$ and $L_y=L_z=(7-9)\sigma$.

Figure 4 shows results for perturbations with $v^{(1)}_{y,\mathrm{sin}}=1.0$ in a system with $L_x=20\sigma$, $L_y=L_z=7\sigma$, and $M_c=10$ cells ($\Delta X=2$). The filled circles in Fig. 4(a) correspond to the main Fourier component of the velocity $\hat{v}^{(1)}_{y,\mathrm{sin}}$ for a calculation using wave number $k=0.31$. The relaxation process is indeed exponential, until the noise-to-signal ratio becomes large enough (around $t>10$) and the observed decay rate $(0.14\pm0.1)\tau^{-1}$ agrees perfectly with the theoretical value of $k^2\eta/\rho^e$. To explicitly appreciate the effect of the hybrid coupling, we show [open circles in Fig. 4(a)] the outcome of a calculation in which the unsteady shear stress contribution to the external force F^{ext} was set to zero, leaving just the contribution of the equilibrium hydrostatic pressure. As expected, if less momentum flux is provided towards P, the decay rate is appreciably slower ($0.07\tau^{-1}$) than the hydrodynamic one ($0.14\tau^{-1}$). Figure 4(b) shows the autocorrelation function (ACF) of $\hat{v}^{(1)}_{y,\mathrm{sin}}(t)$ for another perturbation with a slightly different wave number, $k=0.35$. The good agreement with the theoretical decay [$\exp(-0.17t)$, in dashed line] shows that the scheme is able to deal with small variations in the perturbation shape.

C. Longitudinal perturbations

Longitudinal waves transport mass, momentum, and both mechanical and thermal energy; they are therefore perfectly suited for an overall test of the hybrid scheme behavior. In our setup the wave vector of these waves was perpendicular to the $C\rightarrow P$ interface, and they were generated by imposing mean velocities along the x direction as either pure cosinusoidal, sinusoidal profiles, or combinations of both profiles. As explained before, the particle velocities were extracted from Maxwell-Boltzmann distributions at the local mean velocities and at a constant temperature. The mean velocity profile induces pressure, density, and energy fluctuations with a periodic pattern in the x direction. The temporal behavior of the main flow variables is now described.

1. Mass

One of the main problems involved in the hybrid mass transfer at $C\rightarrow P$ is that although the continuum flux is a floating point number, one can only possibly exchange an integer number of particles. In order to adhere closely as possible to the prescribed continuum mass flux, the following procedure is followed during each interval, $t_C<t\leqslant t_C+\Delta t_C$, $t_C=m\Delta t_C$, $m\in\mathcal{N}$. The first one evaluates the quantity

$$\xi(t_C)\equiv\int_{t_C}^{t_C+\Delta t_C} s(t)\,dt. \tag{42}$$

This floating point number, which represents the number of particles that should cross the $C\rightarrow P$ interface along $t_C<t\leqslant t_C+\Delta t_C$ is converted into an integer $\delta N(t)$ by the following construction:

$$\delta N(t) = NINT[\xi(t_C)] + \delta\xi(t - t_k), \tag{43}$$

$$\delta\xi(t - t_k) = INT\left[\int_{t_k}^{t-\Delta t_P} [\xi(t') - \delta N(t')]dt'\right], \tag{44}$$

where t_k is such that $|\delta\xi(t-t_k)| \leqslant 1$ and $0 = t_0 < t_k < t_{k+1}$. The deviation $\delta\xi(t-t_k)$ assimilates the errors made through successive rounding off ($\xi \rightarrow$ NINT $[\xi]$). When $|\delta\xi(t-t_k)|$ becomes larger than 1 (at $t = \{t_k\}$), a particle is added to (or extracted from) δN and the corrector $\delta\xi$ is then reset to zero. To minimize the effect on the remaining particles over each interval Δt_C, the particle crossings are regularly separated in time at a rate as close as possible to $\delta N(t_C)/\Delta t_C$. As illustrated in Fig. 5, this kind of procedure enables us to follow rather closely the desired mass flux.

2. Momentum

Figures 7–9 show the time dependence of the Fourier components of the main hydrodynamic and thermodynamic variables. Dashed lines correspond to the theoretical trends obtained via the inverse Fourier transform of Eqs. (29)–(35).

For the reasons explained in Sec III A, it is particularly important to ascertain that the averaged velocity at $C \rightarrow P$ correctly follows the desired continuum flow velocity. Figure 6 shows the instantaneous $\overline{v_x}$ and time-averaged velocity $\langle \overline{v_x} \rangle$ at both $C \rightarrow P$ cells. We obtained a very good agreement, the deviation of $\langle \overline{v_x} \rangle$ with respect the continuum value being less than about 5% along most part of the damped oscillation (see Fig. 6). The importance of evaluating the continuum fluxes at precisely the $C \rightarrow P$ interface (x_W in Fig. 1) is illustrated in Fig. 6 by comparison with the outcome of a calculation in which the fluxes are evaluated at $x = x_0$. For this calculation, the deviation with respect to the continuum prescription is clear and its magnitude agrees with the estimate made in Sec. III A $\sim 30\%$.

Figure 7(a) shows the time evolution of the Fourier amplitudes of the velocity in one of the calculations (a pure cosinusoidal perturbation with $\overline{v}^{(1)}_{x,\cos} = 0.6$). The overall velocity $\overline{v}^{(0)}_{x,\cos}$ remains close to zero, confirming that the method conserves the initial total momentum. The $\overline{v}^{(1)}_{x,\sin}$ component (initially set to zero) has been also included to display the level of noise. The ACF of $\overline{v}^{(1)}_x = \overline{v}^{(1)}_{(x,\cos)} + i\overline{v}^{(1)}_{(x,\sin)}$ is shown in Fig. 7(b) for two runs with different initial profiles (for more details see the caption of Fig. 7). These data were fitted to the hydrodynamic expression arising from Eq. (31), and in Fig. 7 these fits are shown with dashed lines. The best fit to the velocity was obtained with $\Gamma k^2 = 0.076$ and $c_s k = 0.867$, while for the ACF it yielded $\Gamma k^2 = 0.072$ and $c_s k = 0.867$. These values coincide, within the error bars, with those imposed by the C flow (obtained upon insertion of the transport coefficients reported in the literature [7]) 0.071 and 0.88, respectively.

3. Thermodynamic variables

We start by observing that, unlike longitudinal momentum and pressure, the relaxation of density, temperature, and energy perturbations includes not only an acoustic part, but also an entropic contribution proportional to $\exp(-\kappa k^2 t)$ [see Eqs. (29)–(39)]. However, as the initial perturbation considered was a mechanical one ($T^{(n)} \simeq 0$), the entropic contribution is rather small. This can be seen in the theoretical expressions written in Fig. 6: the amplitude at $t = 0$ of the entropic part of any heat-related variable is nearly six times smaller than its mechanical counterpart. This observation led us to a more careful study of the effect of heat conduction. As explained in Sec. III C 3, heat currents through each $C \rightarrow P$ cell were created by imposing several (typically two) NHT's placed close to the $C \rightarrow P$ interface over a distance of 4σ. We found it very informative to study the effect of the number p of NHT's per $C \rightarrow P$ cell (notation: p-NHT$_{CP}$) on the collective behavior of the system. In some calculations, this number was reduced to merely 1-NHT$_{CP}$ in such a way that only the local temperature prescribed by the continuum was imposed (and not the heat flux). The results of this comparison may be seen in Figs. 8 and 9. Calculations using 1-NHT$_{CP}$ yielded essentially the same evolution of the velocity and pressure as those with a larger number of NHT's, although the pressure for the 1-NHT$_{CP}$ case showed a slight phase lag, see Fig. 8(d). This is not surprising as $\mathbf{v}$ and P are governed by acoustic terms and are independent of heat transfers. Using 1-NHT$_{CP}$, deviations on ρ^p, e^p, and T^p with respect to the hydrodynamic trend are indeed appreciable, while results with 2-NHT$_{CP}$ adhere closely to the analytical curves (see Fig. 8). In any case, the calculation of the entropy production is the best way to highlight the completely different qualitative behavior of 1-NHT$_{CP}$ with respect to two (or more) NHT$_{CP}$.

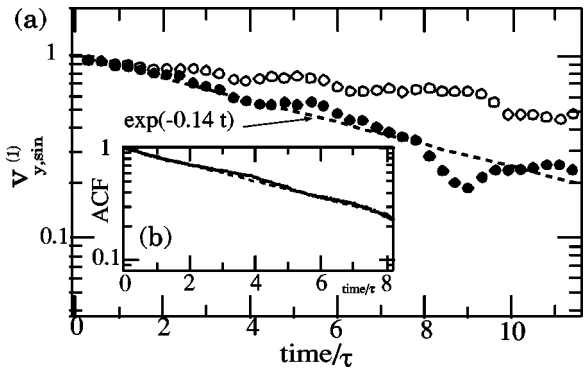

FIG. 4. (a) The main Fourier component of the cell-averaged velocity $v^{(1)}_{y,\sin}$ [in units of σ/τ, with $\tau = (\sigma^2 m/\epsilon)^{1/2}$]. Results correspond to a transversal wave with wave number $k = 0.31$. Comparison is made between a calculation in which the full expression of the external force F^{ext} was imposed (filled circles) and another which did not include the viscous contribution (open circles). The dashed line is the correct hydrodynamic decay. (b) The nondimensional ACF of $\overline{v}^{(1)}_{y,\sin}(t)$ for another transversal perturbation with $k = 0.35$ showing the theoretical decay in the (partially hidden) dashed line. In all cases, the initial amplitude was $\overline{v}^{(1)}_{y,\sin} = 1.0$ and $L_x = 20\sigma$, $L_y = L_z = 7\sigma$. In abscissas, time is nondimensionalized with the LJ reduced time unit $\tau = (\sigma^2 m/\epsilon)^{1/2}$.

4. Entropy

The entropy fluctuation, or more precisely the perturbation of heat $Q^p = T^e s^p$, was calculated using Eq. (27). We

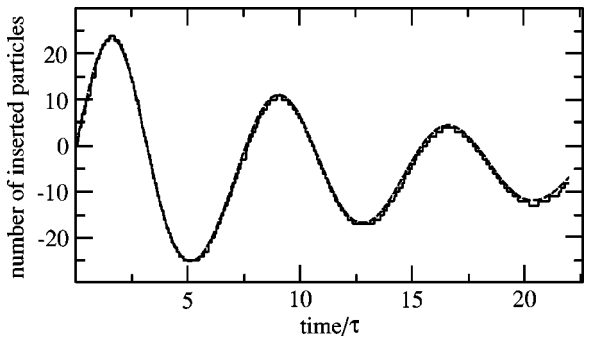

FIG. 5. The total number of inserted particles $\int_0^t \delta N(t')dt'$ at the rightmost $C \rightarrow P$ cell, along a simulation of a longitudinal wave with $k=0.168$ inside a region ($L_x=40\sigma$, $L_y=L_z=9\sigma$) with $\rho^e=0.53$ and $T^e=3.5$. The initial perturbative velocity profile was $u_x=0.60\cos(kx)$. The dashed line is the continuum prescription $\int_0^t s(t')dt'$ (see text). Time has been nondimensionalized with $\tau=(\sigma^2 m/\epsilon)^{1/2}$.

note that, in order to reproduce the steady diffusive heat decay in Eq. (30), an exact cancellation of the acoustic oscillations coming from ρ^p and T^p is necessary [see Eqs. (30) and (29)]. As stated above, the contribution associated with heat diffusion in Eqs. (30) and (29) is rather small as compared to the mechanical one. This observation indicates that

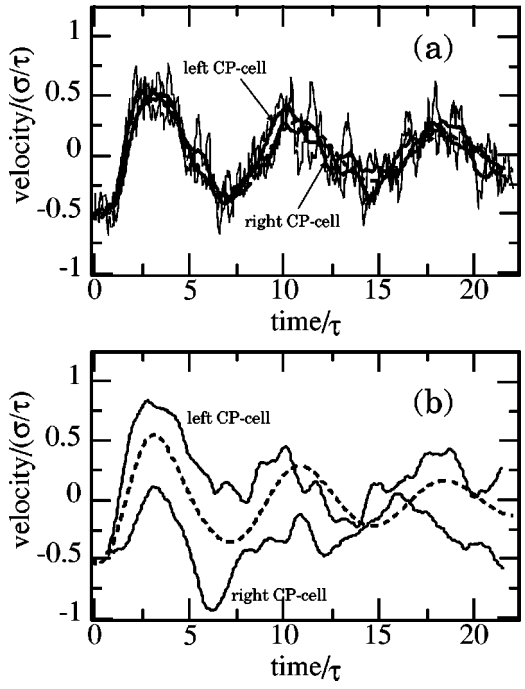

FIG. 6. The velocity at both $C \rightarrow P$ cells for the same parameters as in Fig. 5. The dashed line is the continuum prescription (partially hidden). In (a) we show the outcome of a calculation in which the momentum flux from the C region was evaluated at $x=x_W$ (see Fig. 1); the instantaneous $\overline{v_x}$ velocities are shown in lighter dotted lines, while thicker solid lines are the time-averaged velocities $\langle \overline{v_x} \rangle$. In (b) we show the time-averaged velocities for another calculation with the same parameters as in (a), but evaluating the momentum flux at $x=x_O$. All variables are nondimensionalized with the LJ potential units [σ for length and $\tau=(\sigma^2 m/\epsilon)^{1/2}$ for time].

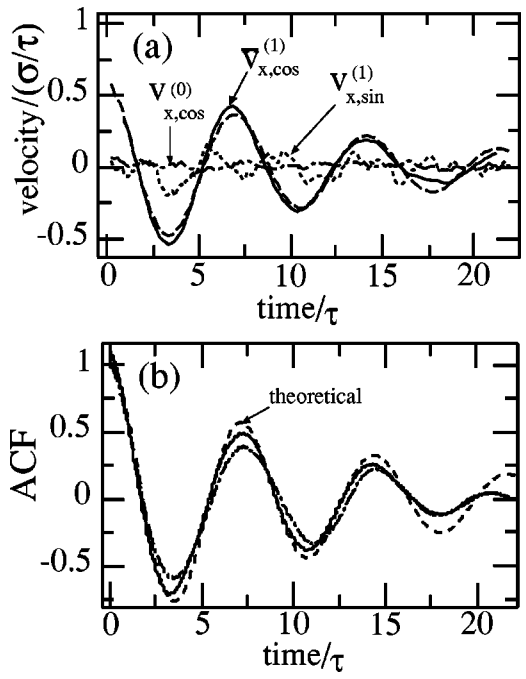

FIG. 7. (a) Time evolution of the Fourier transforms of x velocity $\overline{v}_x^{(n)}$ for the pure cosinusoidal perturbation of Fig. 5. In (b), the nondimensional ACF of $\overline{v}_x^{(1)}(t)$, corresponding to the pure cosinusoidal perturbation (solid line) and to another initial perturbation with $\{\overline{v}_{x,\cos}^{(1)}(0),\overline{v}_{x,\sin}^{(1)}(0)\}=\{0.60,0.25\}$ (dash-dotted line). In (a) and (b), the dashed line is the theoretical hydrodynamic solution. The remaining parameters are the same as those in Fig. 5. Variables are nondimensionalized with the LJ potential units [σ for length and $\tau=(\sigma^2 m/\epsilon)^{1/2}$ for time].

small mechanically driven fluctuations around the local thermodynamic equilibrium may become large enough to alter the purely exponential heat decay. In other words, Eqs. (27) and (34) provide a demanding test of the coupling scheme under the present flow. Figure 9 shows the main Fourier component of the heat perturbation Q^p obtained for 1- and 2-NHT$_{CP}$. The dashed lines correspond to the theoretical expectation. It is evident that the 1-NHT$_{CP}$ case does not obey the second law of thermodynamics at all. On the contrary, a rather good agreement with the theoretical trend is obtained when using at least 2-NHT$_{CP}$. In Fig. 9, it is seen that the behavior measured in the 2-NHT$_{CP}$ case exhibits fluctuations around the theoretical straight line. Typically, the largest excursions last around 3τ from pure exponential decay. As previously stated, they may be due to the weakness of the entropy perturbation, but to confirm this statement we plan in the future to study some heat-driven flows (such as a heat pulse with initial zero mean velocity).

VII. CONCLUSIONS

We have presented the core of a hybrid continuum-particle method for fluids at moderate-to-large densities which couples mass, momentum, and energy transfers between two regions, C and P, described respectively by continuum fluid dynamics and by discrete particle Newtonian dynamics. Both domains

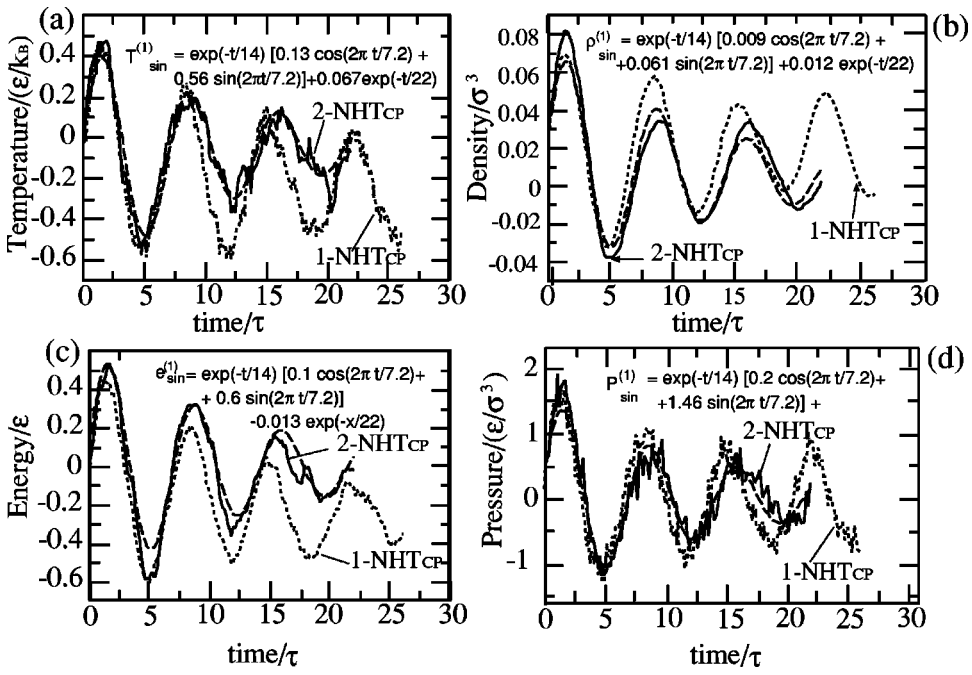

FIG. 8. Time dependence of the Fourier amplitudes of the (a) temperature $\overline{T}^{(1)}_{\rm sin}$, (b) density $\rho^{(1)}_{\rm sin}$ $[=\Sigma_i \exp(ikx_i)/N]$, (c) energy per particle $\overline{e}^{(1)}_{\rm sin}$, and (d) pressure $\overline{P}^{(1)}_{\rm sin}$. All quantities are nondimensionalized with the LJ potential units (σ for length and ϵ for energy). Comparison is made between a simulation with two Nosé-Hoover thermostats per $C\rightarrow P$ cell (2-NHT_{CP}), and another using only one (1-NHT_{CP}, dotted line). In each figure, the analytical hydrodynamic expressions for the dominant Fourier component (in dashed lines) are explicitly written. The initial amplitudes were $\overline{v}^{(1)}_{x,\cos}(0)=0.60$, $\overline{T}^{(1)}_{\rm sin}(0)=-0.06$, $\overline{P}^{(1)}_{\rm sin}(0)=0.25$, and $\rho^{(1)}_{\rm sin}(0)=0.022$.

overlap within a coupling region divided into two subcells which account for the two-way exchange: $C\rightarrow P$ and $P\rightarrow C$. While the procedure at the $P\rightarrow C$ cell is simply to average the particle-based (mass, momentum, and energy) fluxes in order to supply open boundary conditions to the C domain, the operations at the $C\rightarrow P$ cell are much less straightforward as they need to reconstruct a large number of (particles') degrees of freedom only from the knowledge of the three fluxes of conserved quantities arising within C. The present work has been concerned with extending the $C\rightarrow P$ coupling to arbitrary rates of mass, momentum, and energy transfer. To this end, the proposed method has been tested under unsteady flows which demand conformance to the whole set of conserved variable densities. In particular, we have considered the set of relaxing flows arising from hydrodynamics, namely longitudinal and transversal waves. We have followed the idea proposed by Flekkoy *et al.* [5], in the sense that the scheme is explicitly based on direct flux exchange between the C and P regions. In order to deal with unsteady scenarios, we have shown that the fluxes injected into the particle region from the continuum region need to be measured exactly at the $C\rightarrow P$ interface and not at the nodes of the continuum lattice.

The implementation of flux exchanges requires the supply of energy currents to the particle system arising from the C domain due to advection, dissipation, and conduction. To inject the correct amount of advected energy, the particle-averaged specific energy at the $C\rightarrow P$ cell needs to be equal to the continuum value. This can only be achieved if the new inserted particles are placed at positions where the (interparticle) potential energy equals the C-specified internal energy per unit mass. This severe condition has been implemented by the USHER algorithm, whose purpose is twofold: to provide the correct mass transfer rate and to ensure the balance of energy advection. In the proposed scheme, the balance of energy dissipation arises naturally, provided that the cell-averaged velocity and the injected momentum flux equal their continuum counterparts. This is made possible by applying the external force according to a flat distribution, instead of a biased one as used by Flekkoy *et al.* [5] but as a result, the new particles have to be inserted within a nonvanishing density environment. This is sorted out by the USHER in a very efficient way. Energy conduction has been implemented by using a set of Nosé-Hoover thermostats adjacent to the $C\rightarrow P$ interface, whose temperature and position are determined through the continuum local temperature gradient. Confirmation of the validity of this procedure is obtained from the correct rate of entropy production computed in our simulations of longitudinal waves. We showed that using only one thermostat per $C\rightarrow P$ cell (i.e., providing only the local value of T but not the heat flux) leads to negative entropy production. Therefore, in the context of energy transfer, this result reinforces the central importance of coupling through fluxes proposed by Flekkoy *et al.* [5].

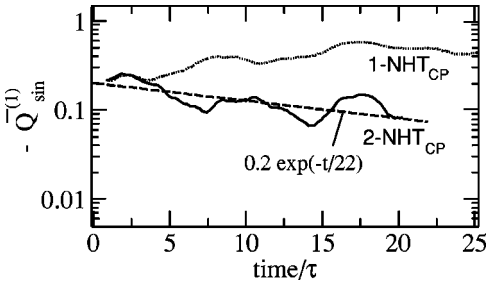

FIG. 9. The main Fourier amplitude of the heat density perturbation $-\langle\overline{Q}^{(1)}_{\rm sin}\rangle(t)$ time-averaged along $\Delta t_C=1.0$ (and multiplied by -1). The parameters are the same as those of Fig. 5 (and 8) and heat density is in units of ϵ/σ^3. The dashed line corresponds to the theoretical decay. Comparison is made between two (2-NHT_{CP}) and one (1-NHT_{CP}) Nosé-Hoover thermostats per $C\rightarrow P$ cell. The latter violates the second law of thermodynamics.

Enhancements to the present scheme are under investigation and merit some discussion here. The number density at $C \rightarrow P$ may be controlled by a feedback algorithm which preserves the momentum flux balance. Other kinds of implementations for the energy transport by conduction also deserve to be considered. Finally, we plan to implement the $P \rightarrow C$ coupling in conjunction with a finite volume CFD solver in 3D. In order to extend the coupling scheme to higher dimensions, some additional complications will need to be adressed. First, a mass flux will be assigned to each cell within an array of neighboring $C \rightarrow P$ cells. To adhere to mass continuity, particles will then have to be inserted within precisely defined finite regions and the insertion algorithm may have to pay an extra computational cost for this restriction of the search domain. We have checked, however, that the distance traveled by the USHER algorithm from the initial trial position to the final insertion site is rather small [11] (typically, less than 1σ and less than 0.5σ on average) so we do not expect any significant extra cost if the search for insertion sites is done within volumes larger than $(2\sigma)^3$. In higher dimensions, one may also have to smooth to some extent the variations of the mean mechanical quantities imposed along the $C \rightarrow P$ region. To this end, it may be necessary to interpolate the external force along neighboring $C \rightarrow P$ cells in such a way that the local momentum flux imposed at each $C \rightarrow P$ cell is still preserved. In the same way, although the Maxwell distribution, used here to choose the velocities of the new particles, proved to be sufficient to ensure momentum continuity for 1D coupling (i.e., with no neighboring $C \rightarrow P$ cells), it may be convenient to use a Chapman-Enskog distribution in higher dimensions. This latter distribution enables the average velocity of the inserted particles to conform to the velocity gradient along neighboring $C \rightarrow P$ cells. We hope to report our findings in these areas in future publications.

ACKNOWLEDGMENTS

We gratefully acknowledge fruitful discussions with E. Flekkoy, P. Español, G. Ciccotti and R. Winkler and useful comments from B. Boghosian, A. Ladd and I. Paganobarraga. This research was supported through a European Community Marie Curie Grant No. HPMF-CT-2001-01210. R.D.-B. wishes also to acknowledge support from Project No. BFM2002-0290.

[1] A. Garcia, J. Bell, Wm.Y. Crutchfield, and B. Alder, J. Comput. Phys. **154**, 134 (1999).

[2] S.T. O'Connell and P.A. Thompson, Phys. Rev. E **52**, R5792 (1995).

[3] N. Hadjiconstantinou and A. Patera, Int. J. Mod. Phys. C **8**, 967 (1997); N.G. Hadjicostantinou, Phys. Rev. E **59**, 2475 (1999).

[4] J. Li, D. Liao, and S. Yip, Phys. Rev. E **57**, 7259 (1998).

[5] E.G. Flekkoy, G. Wagner, and J. Feder, Europhys. Lett. **52**, 271 (2000).

[6] K. Johnson, J.A. Zollweg, and K.E. Gubbins, Mol. Phys. **78**, 591 (1993).

[7] D.M. Heyes, Chem. Phys. Lett. **153**, 319 (1988).

[8] P. Borgelt, C. Hoheisel, and G. Stell, Phys. Rev. A **42**, 789 (1990).

[9] D.J. Evans and G.P. Morris, *Statistical Mechanics of Nonequilibrium Liquids* (Academic Press, London, 1990).

[10] Frenkel and B. Smith, *Understanding Molecular Simulations* (Academic Press, London, 1996).

[11] R. Delgado-Buscalioni and P.V. Coveney, J. Chem. Phys. (to be published).

[12] After submission but prior to publication of this paper we have implemented further improvement in the USHER algorithm. The new USHER scheme, to appear in Ref. [11], reduces the number of iterations to 8–30 for densities within the range $\rho = 0.5–0.8$.

[13] C. Trozzi and G. Ciccotti, Phys. Rev. A **29**, 916 (1984); A. Tenenbaum, G. Ciccotti, and Renato Gallico, *ibid.* **25**, 2778 (1982).

[14] J.P. Hansen and I.R. McDonald, *Theory of Simple Liquids* (Academic Press, London, 1986).

[15] D.J. Tritton, *Physical Fluid Dynamics* (Oxford University Press, Oxford, 1988).